Electronic Supporting Information (ESI)

Development of Thermally Stable FTO Thin Films on Quartz Substrates for Carrier Collection in Semiconductor Photoelectrodes

Tomohiro Higashi,[a] Shintaro Fukagawa,[b] Kaisei Wakishima,[b] Koichi Yoshiyama,[b] Yuki Narita,[b] and Kenji Yoshino*[b]*

[a] T. Higashi, Institute for Tenure Track Promotion, University of Miyazaki, 1-1 Gakuen-kibanadai-nishi, Miyazaki 889-2192, Japan.

[b] S. Fukagawa, K. Wakishima, K. Yoshiyama, Y. Narita, and K. Yoshino, Electrical and Electronic Engineering Program, Faculty of Engineering, University of Miyazaki, 1-1 Gakuen-kibanadai-nishi, Miyazaki 889-2192, Japan.

*E-mails: t_higashi@cc.miyazaki-u.ac.jp , t0b114u@cc.miyazaki-u.ac.jp

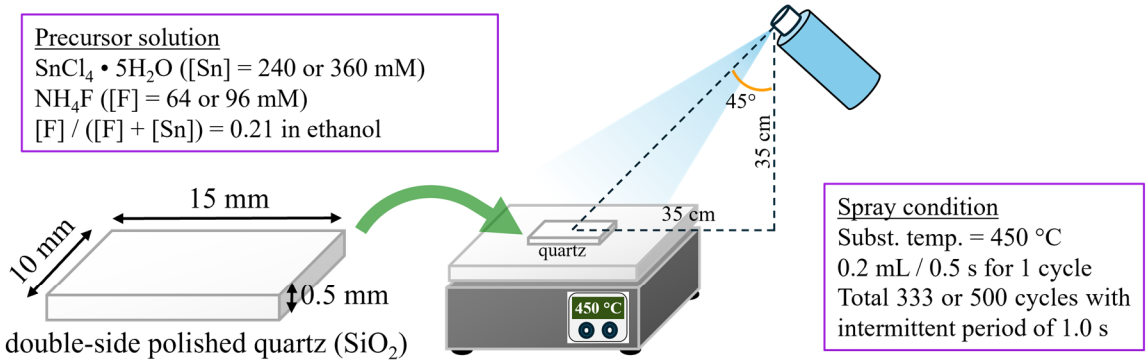

	$[Sn^{4+}]$	$[F^{-}]$	Spray cycles
Sample A	240 mM	64 mM	500
Sample B	360 mM	96 mM	333

Figure S1. Fabrication process of F-doped SnO_2 (FTO) on double-side polished quartz (SiO_2) substrate.

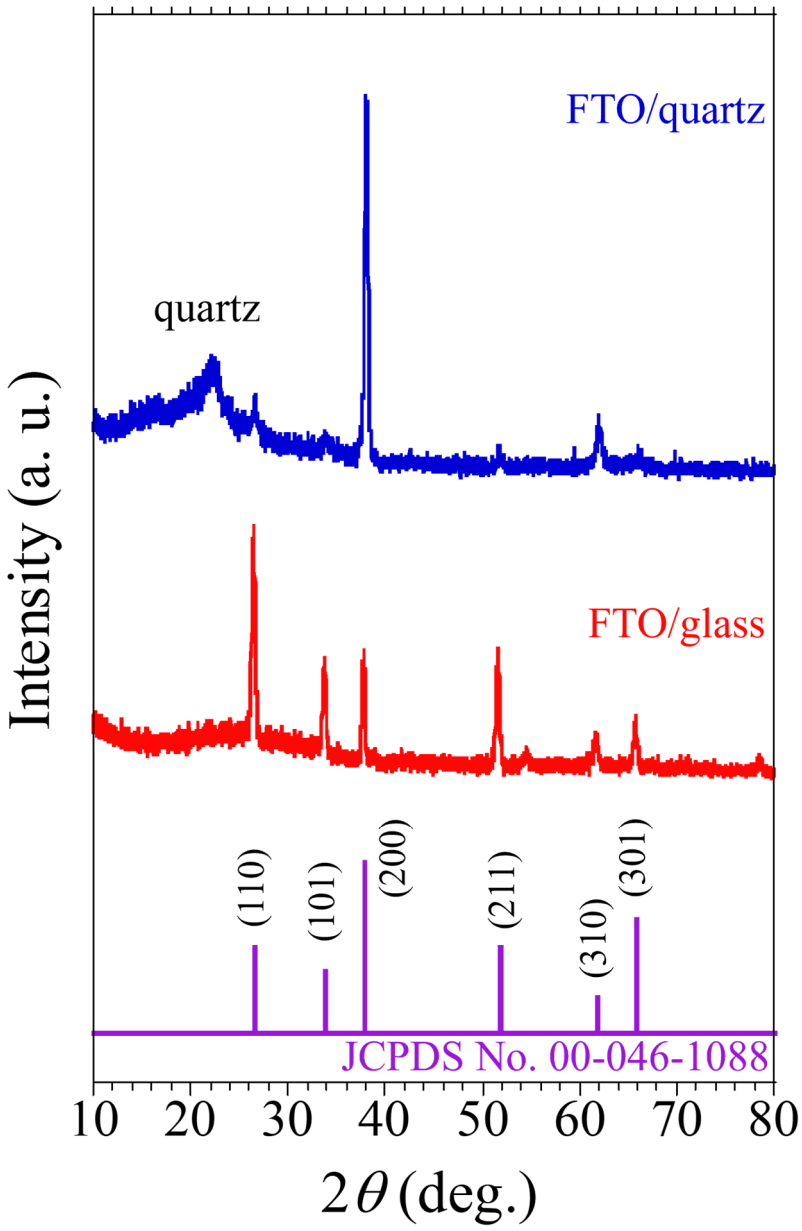

Figure S2. X-ray diffraction (XRD) patterns of FTO/quartz prepared through a spray pyrolysis method and FTO/glass reference (type-VU, AGC). The solid lines colored in purple indicate the reference XRD pattern of SnO_2 (JCPDS No. 00-046-1088). The full width at half maximum of the (110) and (200) for FTO/glass reference are 0.38° and 0.31°, respectively.

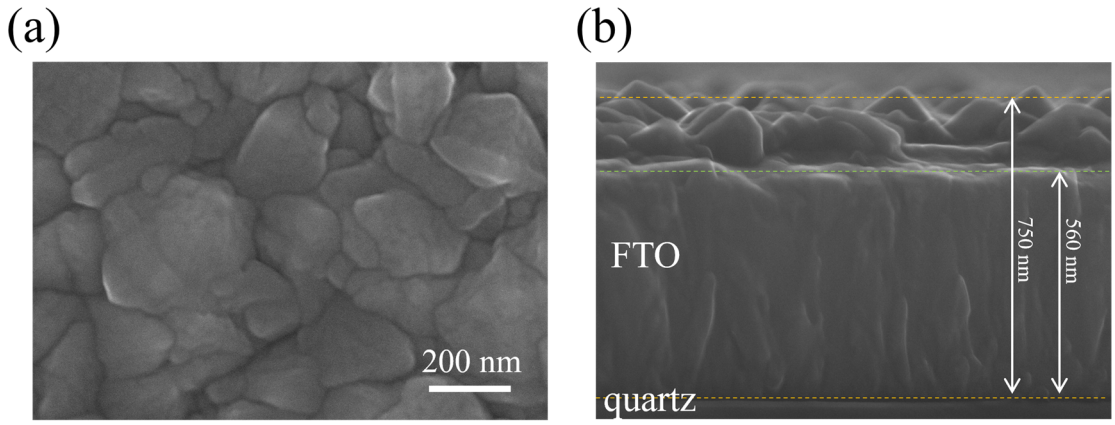

Figure S3. (a) Top-view and (b) cross-sectional scanning electron microscopy (SEM) images of FTO/quartz prepared through spray pyrolysis methods using a precursor solution for sample B.

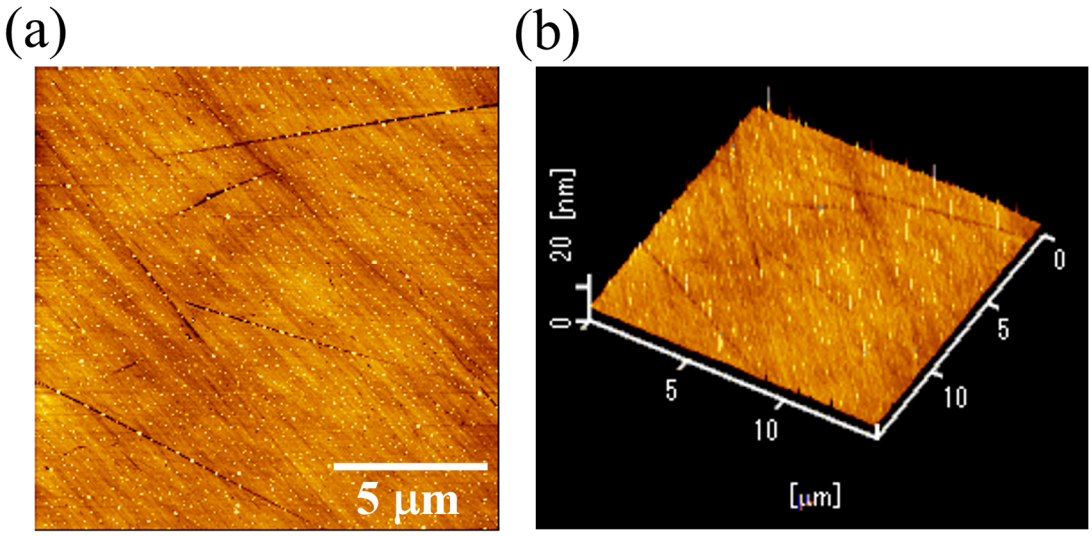

Figure S4. Atomic force microscopy (AFM) top-view (a) and 3D-images (b) of bare-quartz substrate. AFM image of the quartz indicated a flat surface topography in the range of tens of micrometers. The average surface roughness was found to be 0.495 nm and the maximum depth of the grooves seen in the AFM image was found to be 5.1 nm.

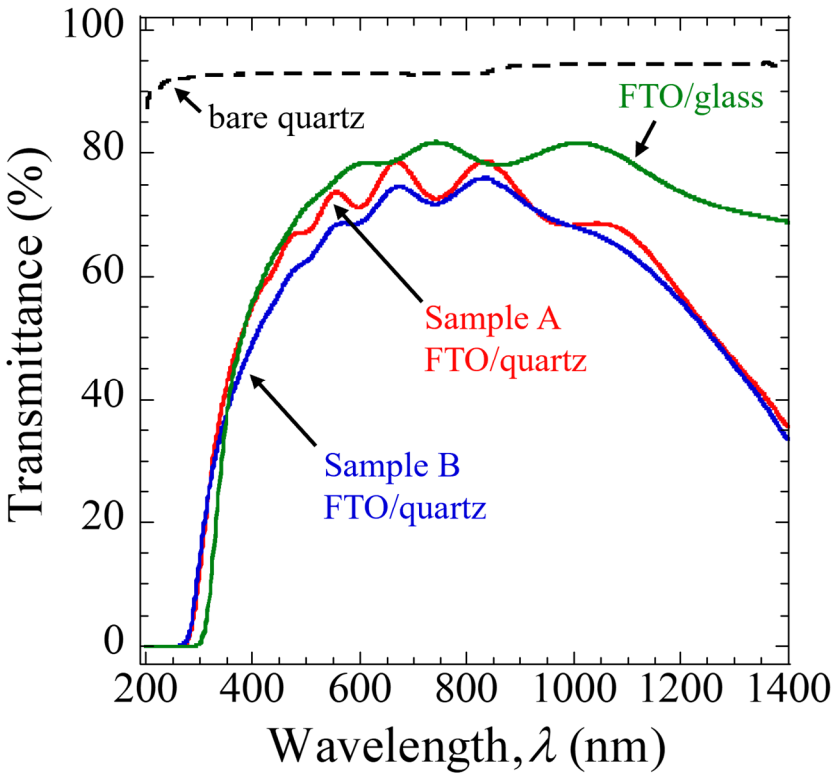

Figure S5. UV-Vis-NIR transmission spectra for FTO/quartz (sample A colored in red, and sample B colored in blue), FTO/glass reference (colored in green), and bare quartz substrate (dashed line).

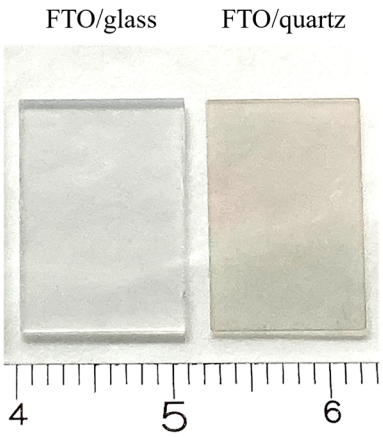

Figure S6. Photograph of FTO/glass (left) and FTO/quartz (right) samples.

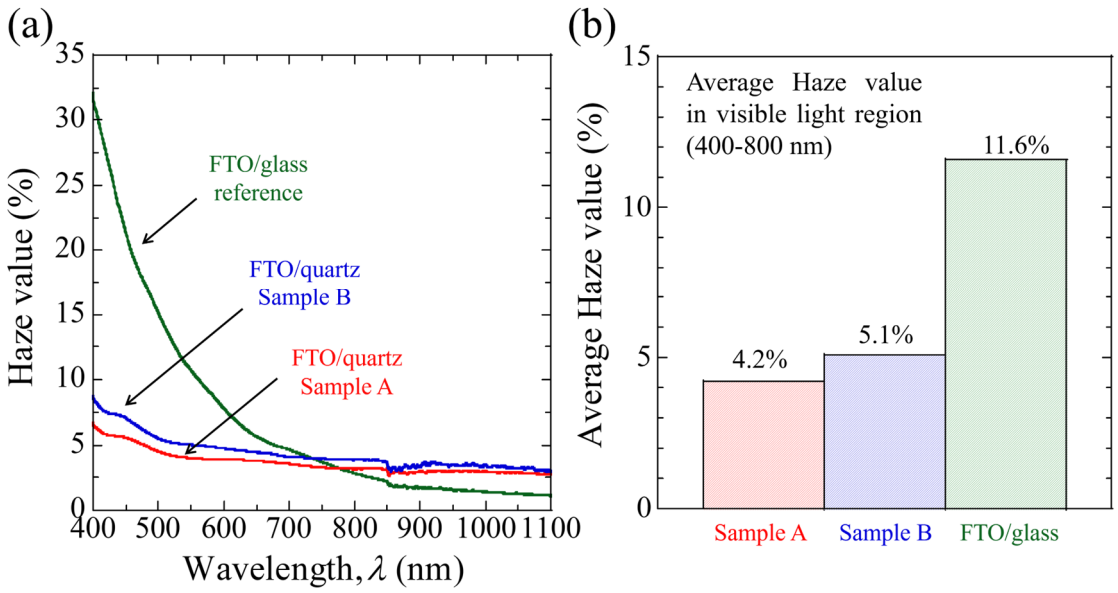

Figure S7. (a) Haze value of FTO/quartz sample A (colored in red), sample B (colored in blue), and FTO/glass reference (colored in green) as a function of light wavelength (λ). (b) The average Haze value of the samples at the wavelength ranges from 400 nm to 800 nm. The Haze value was calculated by the following the equation, Haze value (%) = $[(T_4/T_2) - (T_3/T_1)] \times 100$, where T_1, T_2, T_3, and T_4 are transmittance of baseline spectrum obtained using a white diffuse plate, the total light transmittance of the sample, light scattering in transmittance of equipment, light scattering in transmittance of the sample, respectively.

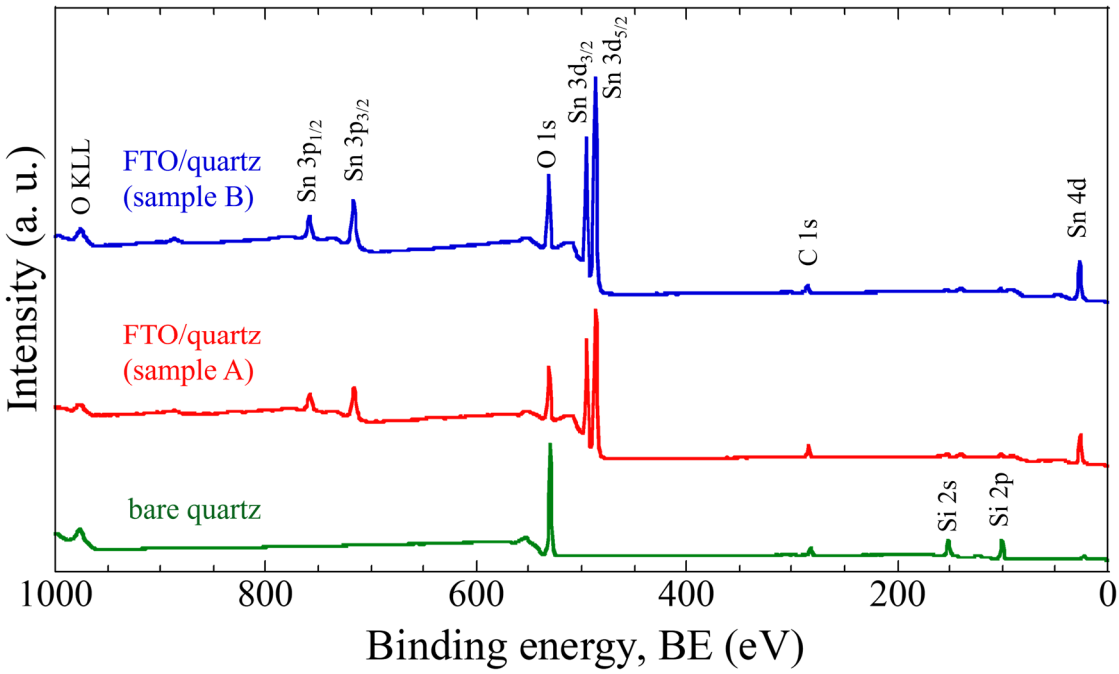

Figure S8. X-ray photoelectron spectroscopy (XPS) overall spectra (wide-scan XPS) of FTO/quartz (sample A colored in red and sample B colored in blue) and bare quartz substrate.

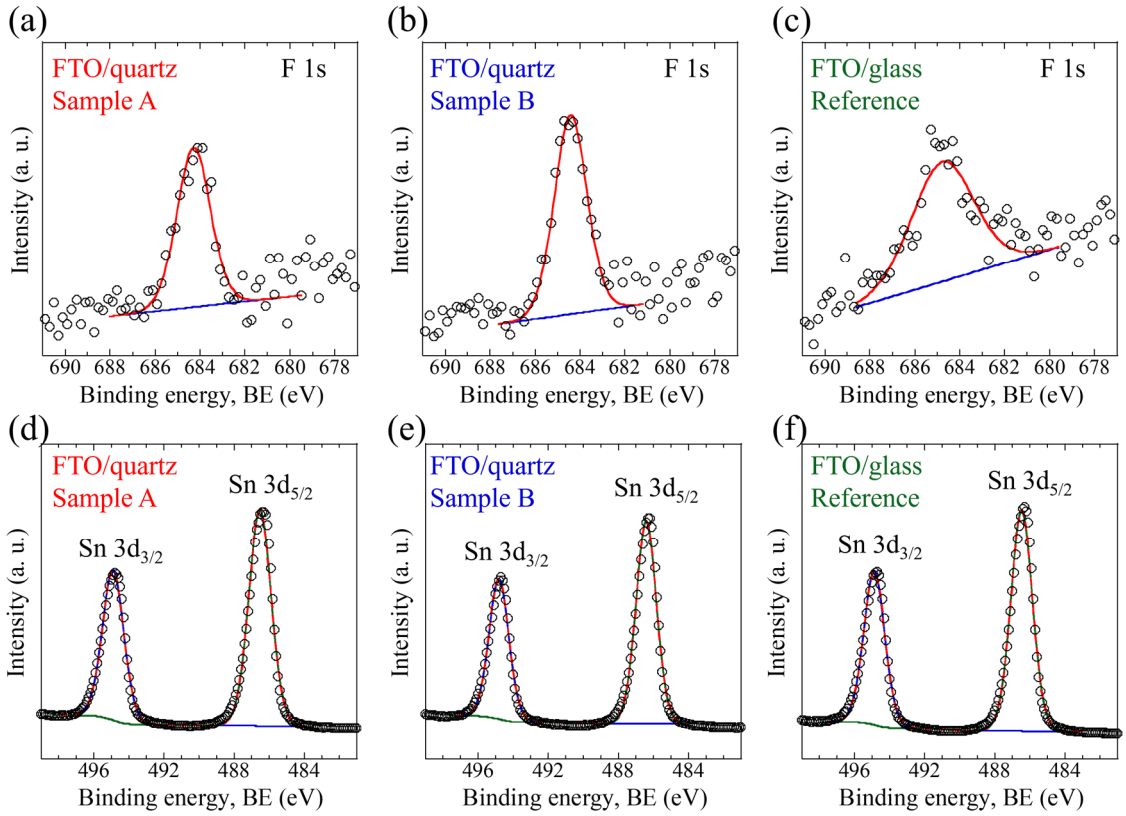

Figure S9. High-resolution XPS (HR-XPS) spectra of F 1s (a-c) and Sn 3d (d-f) for FTO/quartz sample A (a, d), FTO/quartz sample B (b, e), and FTO/glass reference (c, f). In panels (a-c), empty circle, solid red line, and solid blue line indicate experimental data, fitted curve, and baseline for data fitting, respectively. In panels (d-f), empty circle, solid line (blue and green), and dashed line (red) indicate experimental data, fitted curves, and composite curves used in peak fitting, respectively.

Table S1. Surface concentration ratio of F^- and Sn^{4+} from the HR-XPS spectra*

	F / (F + Sn)	Sn / (F + Sn)
Sample A	1.4%	98.6%
Sample B	1.5%	98.5%
FTO/glass reference	1.5%	98.5%

* Surface atomic concentration ratio of F and Sn of FTO/quartz and FTO/glass was calculated using the results of HR-XPS peak fitting for the F 1s (peaked at 684.4 eV) and Sn 3d (peaked at 486.2 and 494.6 eV) as shown in Figure S9.

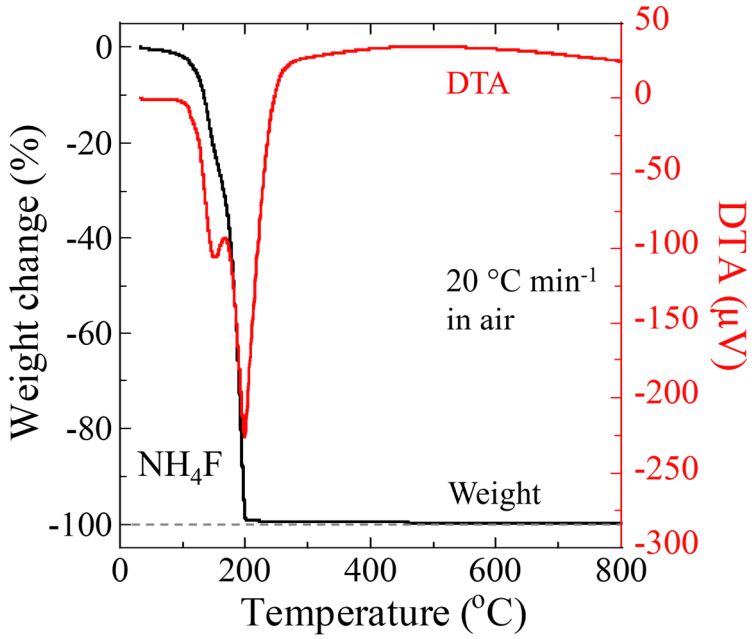

Figure S10. Thermogravimetry-differential thermal analysis (TG-DTA) data of NH_4F. The TG-DTA data was acquired in the air at the temperature ramp of 20 °C min^{-1}.

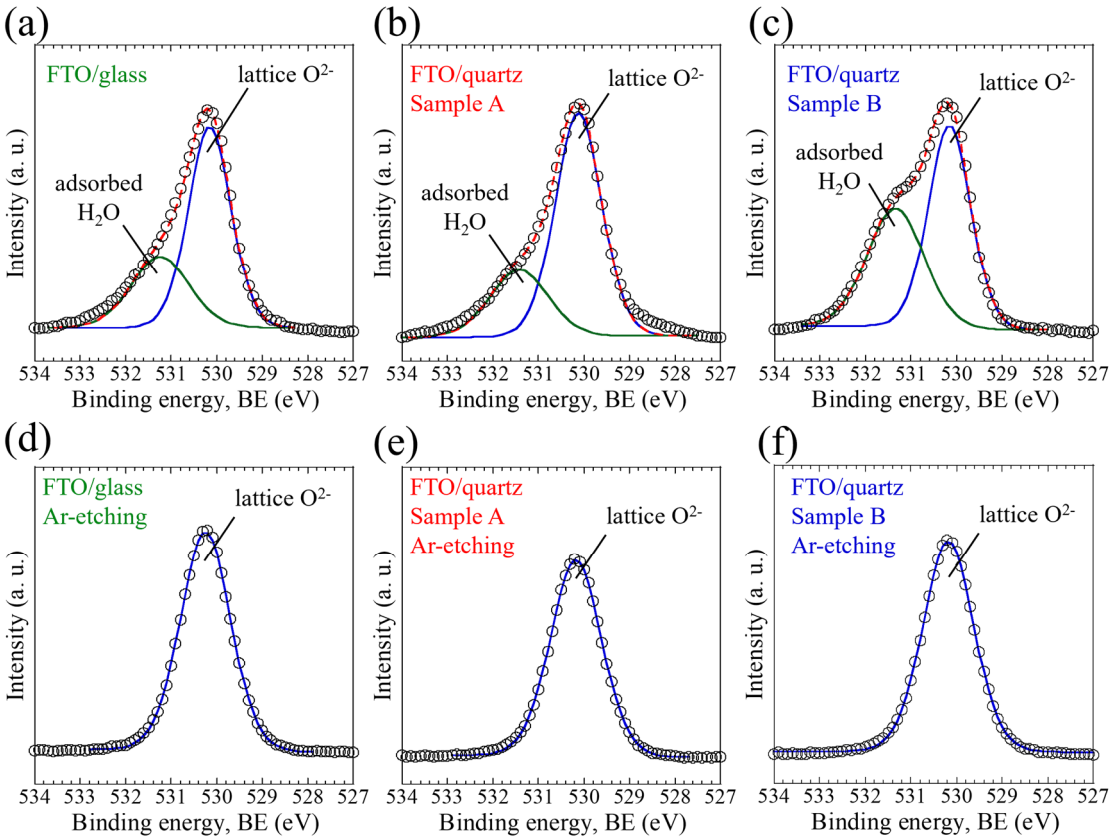

Figure S11. HR-XPS O 1s spectra before (a-c) and after (d-f) Ar-etching treatment for FTO/glass reference (a, d), FTO/quartz sample A (b, e), and FTO/quartz sample B (c, f). In panels (a-c), empty circle, solid line (blue and green), and dashed line (red) indicate experimental data, fitted curves for lattice O^{2-} and adsorbed H_2O, and composite curves used in peak fitting, respectively. In panels (d-f), empty circle and solid blue line indicate experimental data and fitted curve for lattice O^{2-}, respectively.

Table S2. Surface concentration ratio of F^- and O^{2-} from the HR-XPS spectra*

	F / (F + O)	O / (F + O)
Sample A	1.1%	98.9%
Sample B	1.3%	98.7%
FTO/glass reference	1.3%	98.7%

* Surface atomic concentration ratio of F and O of FTO/quartz and FTO/glass was calculated using the results of HR-XPS peak fitting for the F 1s (peaked at 684.4 eV) and O 1s (peaked at 530.2 eV assigned as lattice O^{2-}) as shown in Figures S9a-c and S11d-f.

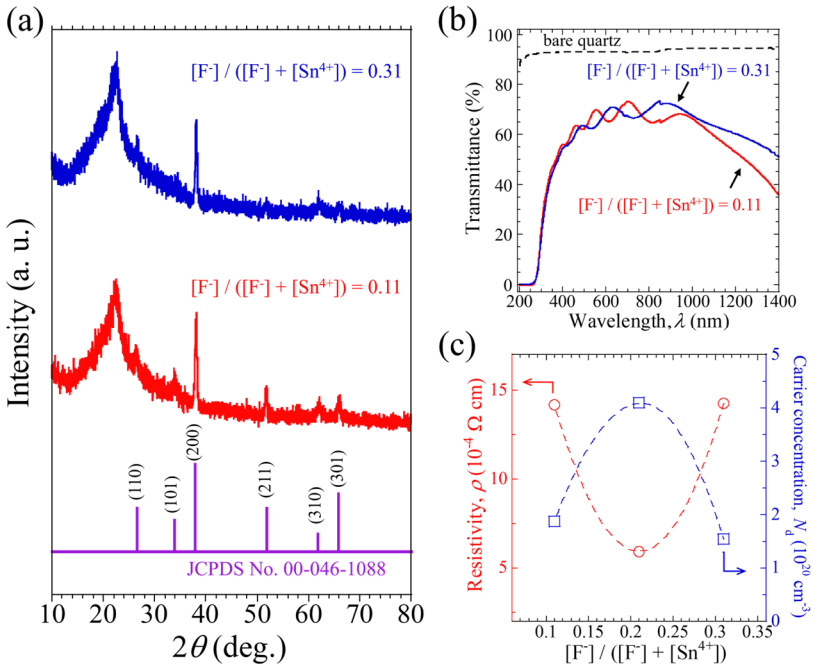

Figure S12. Characterization of FTO/quartz prepared by spray pyrolysis using different molar concentration ratios, $[F^-]$ / ($[F^-]$ + $[Sn^{4+}]$), adjusted to 0.11 and 0.31. (a) XRD patterns of FTO/quartz for samples 0.11 (red) and 0.31 (blue). (b) UV-Vis-NIR transmission spectra for FTO/quartz, samples 0.11 (red) and 0.31 (blue), and bare quartz substrate (dashed line colored in black). (c) Plot of resistivity (ρ) and carrier concentration (N_d) of FTO/quartz samples prepared by spray pyrolysis using different molar concentration ratios ($[F^-]$ / ($[F^-]$ + $[Sn^{4+}]$)) precursor solutions.

Table S3. Electric properties of FTO/quartz and FTO/glass at room temperature.

	σ (Ω^{-1} cm^{-1})	ρ (Ω cm)	N_d (cm^{-3})	μ_H (cm^2 V^{-1} s^{-1})	FTO thickness
Sample A	$(1.7 \pm 0.1) \times 10^3$	$(5.9 \pm 0.1) \times 10^{-4}$	$(4.1 \pm 0.1) \times 10^{20}$	24.8 ± 2.5	650 nm
Sample B	$(2.0 \pm 0.1) \times 10^3$	$(5.0 \pm 0.1) \times 10^{-4}$	$(4.9 \pm 0.2) \times 10^{20}$	25.7 ± 3.0	750 nm
FTO/glass reference	$(1.9 \pm 0.1) \times 10^3$	$(5.4 \pm 0.1) \times 10^{-4}$	$(2.3 \pm 0.1) \times 10^{20}$	50.0 ± 2.2	600 nm
FTO/glass[1]	–	6.0×10^{-4}	4.0×10^{20}	29.0	660 nm
FTO/glass[2]	–	4.0×10^{-4}	4.7×10^{20}	34	420-490 nm

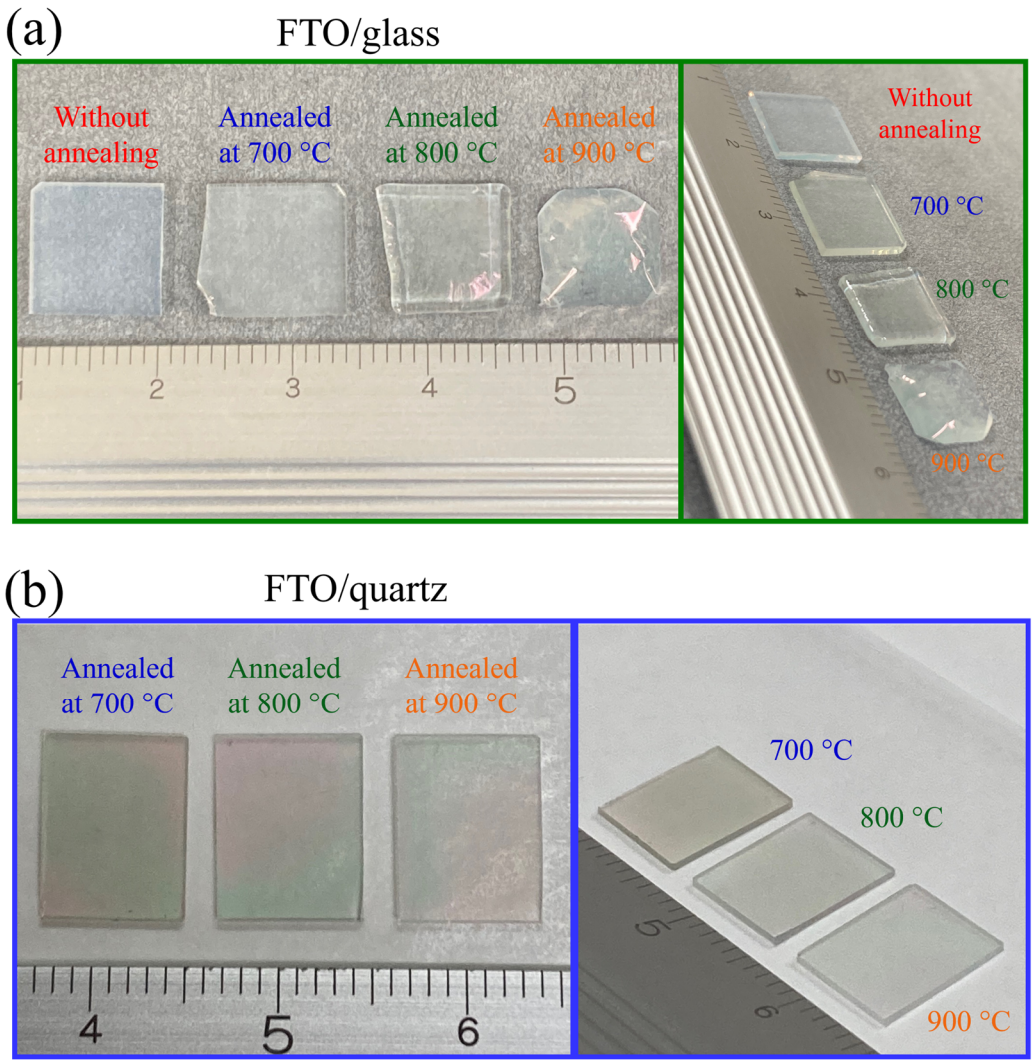

Figure S13. Photographs of (a) FTO/glass reference and (b) FTO/quartz processed with a post-annealing treatment in air at temperatures of 700 °C, 800 °C, and 900 °C for 1 h.

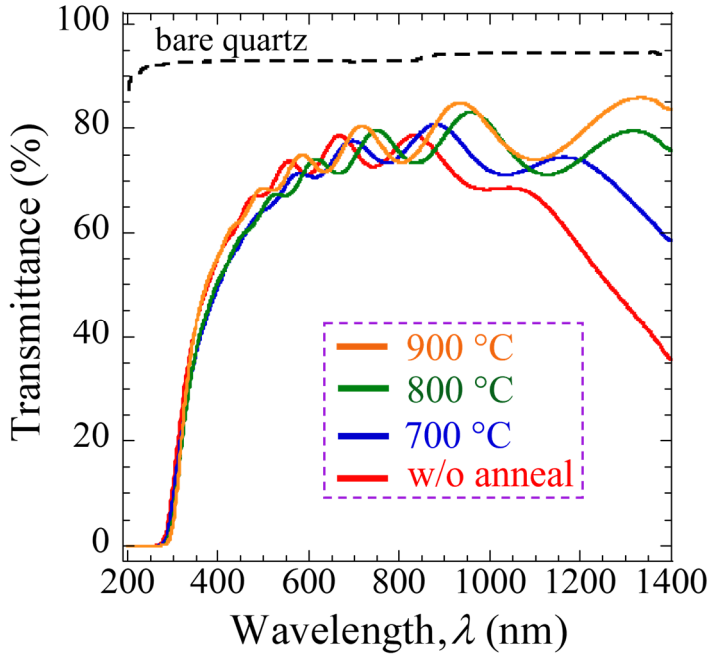

Figure S14. UV-Vis-NIR transmission spectra for FTO/quartz (sample A) processed with post-annealing treatment at temperatures of 700 °C (blue), 800 °C (green), and 900 °C (orange). The solid red line represents the transmission spectrum of raw FTO/quartz (without annealing), and the dashed black line corresponds to the bare quartz substrate.

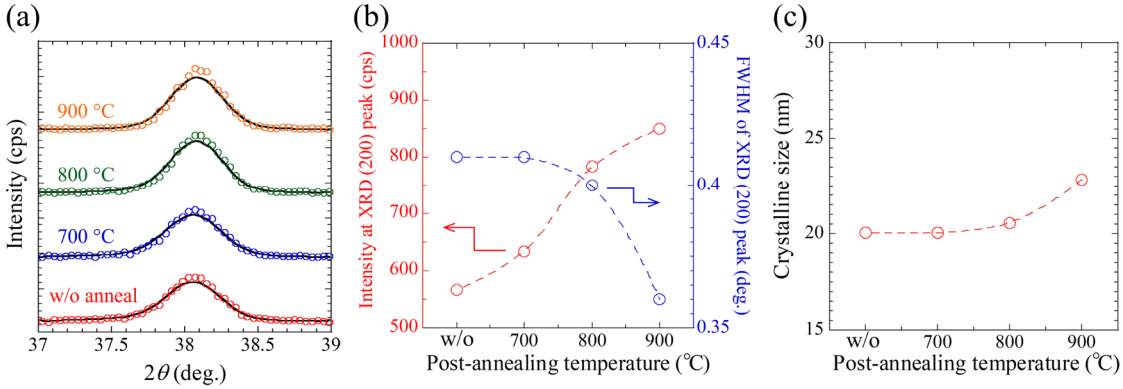

Figure S15. (a) XRD (200) peak of FTO/quartz before (red) and after annealing at 700 °C (blue), 800 °C (green), and 900 °C (orange). (b) Plot of the intensity of XRD (200) peak and full-width half maximum (FWHM) as a function of post-annealing temperature. (c) Plot of crystalline size (D) of FTO before and after post-annealing treatment. In panel (c), the data was derived from panel (b) and calculated using Sherrer's formula: $D = 0.9\lambda / B\cos\theta_B$, where λ, B and θ_B are the X-ray wavelength (Cu Kα, 0.15418 nm), FWHM (rad.), and Bragg's diffraction angle (deg.), respectively.[2]

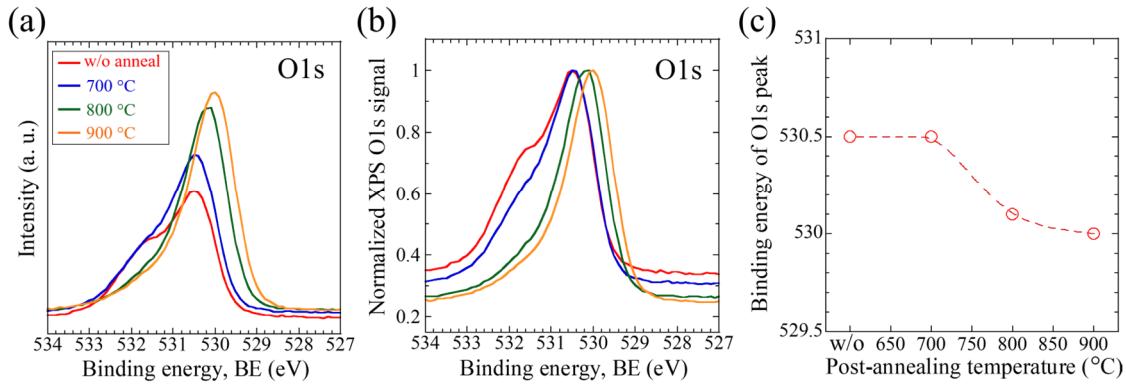

Figure S16. HR-XPS O 1s spectra before Ar-etching treatment for pristine-FTO/quartz (red) and FTO/quartz processed with the post-annealing treatment at the temperatures of 700 °C (blue), 800 °C (green), and 900 °C (orange) in the air for 1 h. (a) HR-XPS O 1s spectra. (b) Normalized HR-XPS O 1s spectra at the main peak attributed to the O^{2-} XPS peak. (c) A plot of binding energy of O 1s main peak as a function of the post-annealing temperatures.

Table S4. Fitting parameters for HR-XPS spectra of F 1s, Sn 3d, and O1s of FTO/quartz.

	Binding energy, BE (eV)		Full width half maximum, FWHM (eV)	
	F 1s		F 1s	
F^-	684.4		1.70	
	Sn $3d_{5/2}$	Sn $3d_{3/2}$	Sn $3d_{5/2}$	Sn $3d_{3/2}$
Sn^{4+}	486.2	494.6	1.35	1.35
	O 1s		O 1s	
lattice O^{2-}	530.2		1.30	
adsorbed H_2O	531.5		1.50	

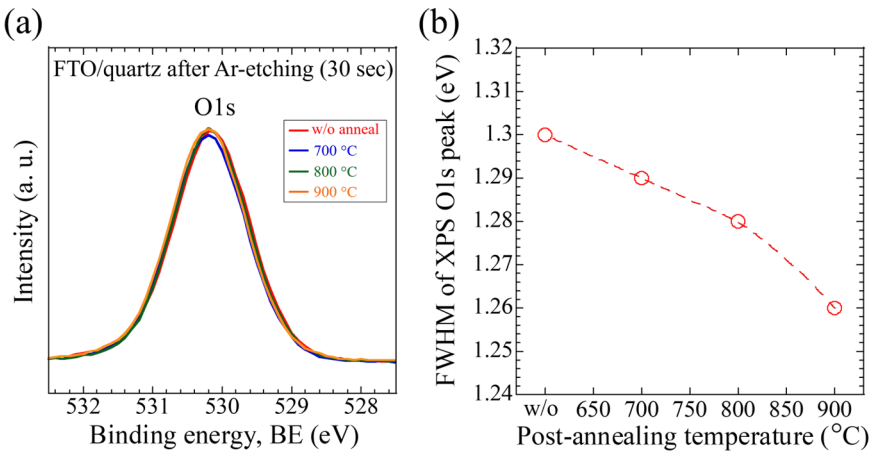

Figure S17. (a) HR-XPS O 1s spectra after Ar-etching treatment for thirty seconds for FTO/quartz samples before (w/o anneal) and after post-annealing treatment (700 °C, 800 °C, and 900 °C for 1 h). (b) A plot of the FWHM of XPS O 1s peak at the BE of 530.2 eV attributable to the lattice O^{2-} XPS peak.

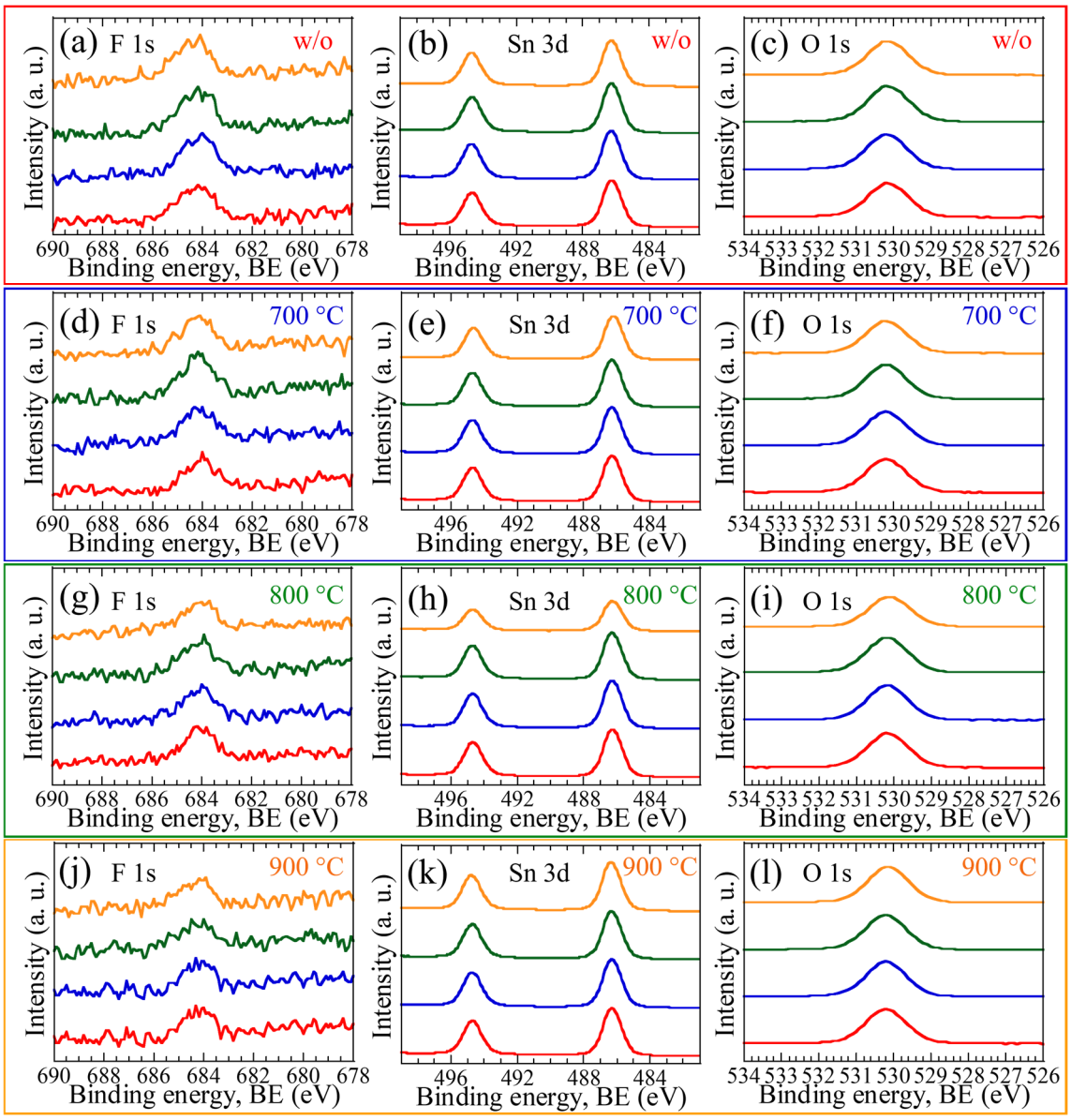

Figure S18. HR-XPS spectra after Ar-etching treatment over 30 sec (in red), 90 sec (blue), 450 sec (green), and 1080 sec (orange) of FTO/quartz before (a-c) and after post-annealing treatment at the temperature of 700 °C (d-f), 800 °C (g-i), and 900 °C (j-l). In panels (a, d, g, and j), (b, e, h, and k), (c, f, i, and l) correspond to the XPS spectra of F 1s, Sn 3d, and O 1s, respectively.

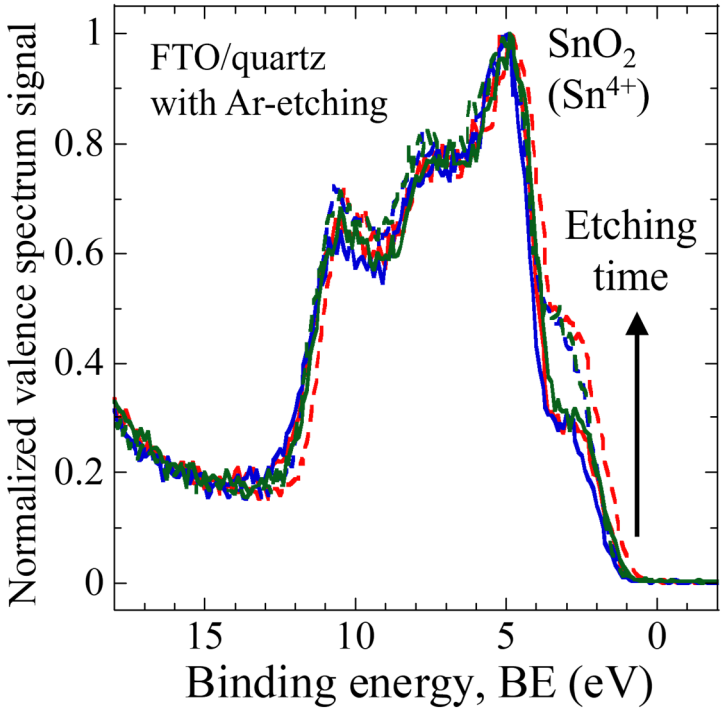

Figure S19. Normalized valence spectra after Ar-etching treatment of FTO/quartz (sample A). With increasing the etching time, the tailing on the spectra due to the formation of reduced SnO_2 species increased together with oxygen vacancy inside the FTO.

Table S5. Raman peaks observed on the FTO/quartz before and after the annealing treatment.

	A_{1g}	B_{2g}	A_{2u}	$E_u(\nu_{TO})$	$Eu(\nu_{LO})$
w/o anneal	627.2 cm^{-1}	776.0 cm^{-1}	686 cm^{-1}	243.6 cm^{-1}	281.2 cm^{-1}
700 °C	627.2 cm^{-1}	776.0 cm^{-1}	686 cm^{-1}	243.6 cm^{-1}	284.1 cm^{-1}
800 °C	627.8 cm^{-1}	775.0 cm^{-1}	—	243.4 cm^{-1}	284.1 cm^{-1}
900 °C	628.1 cm^{-1}	775.1 cm^{-1}	—	—	—

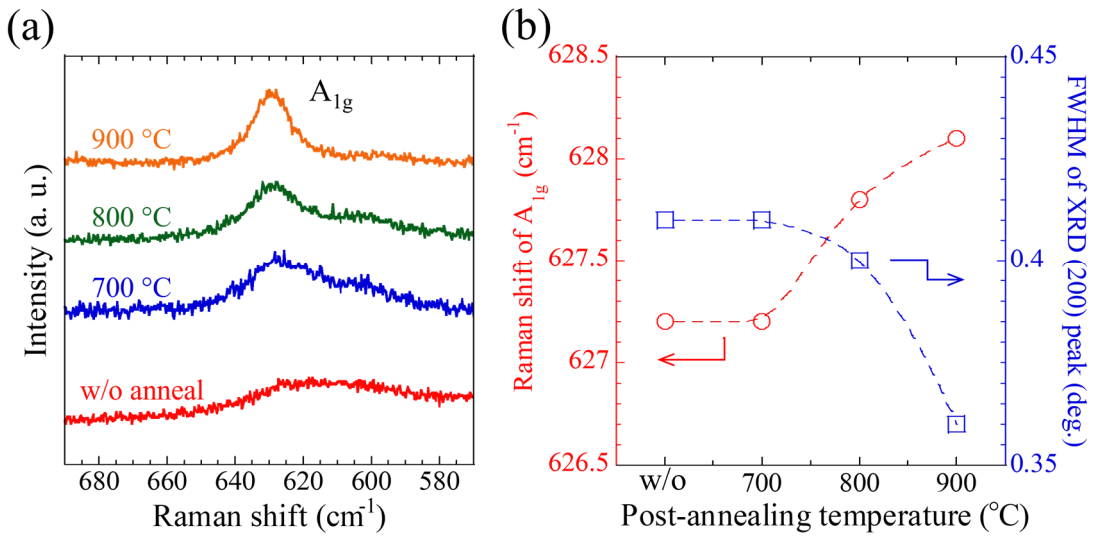

Figure S20. (a) Raman spectra of FTO/quartz without post-annealing (red), FTO/quartz with post-annealing at 700 °C (blue), 800 °C (green), and 900 °C (orange). (b) Plots of Raman shift of A1g mode and FWHM of XRD (200) peak as a function of the post-annealing temperature. The data of Raman shift and FWHM were derived from Fig. S20a and Fig. S15a, respectively.

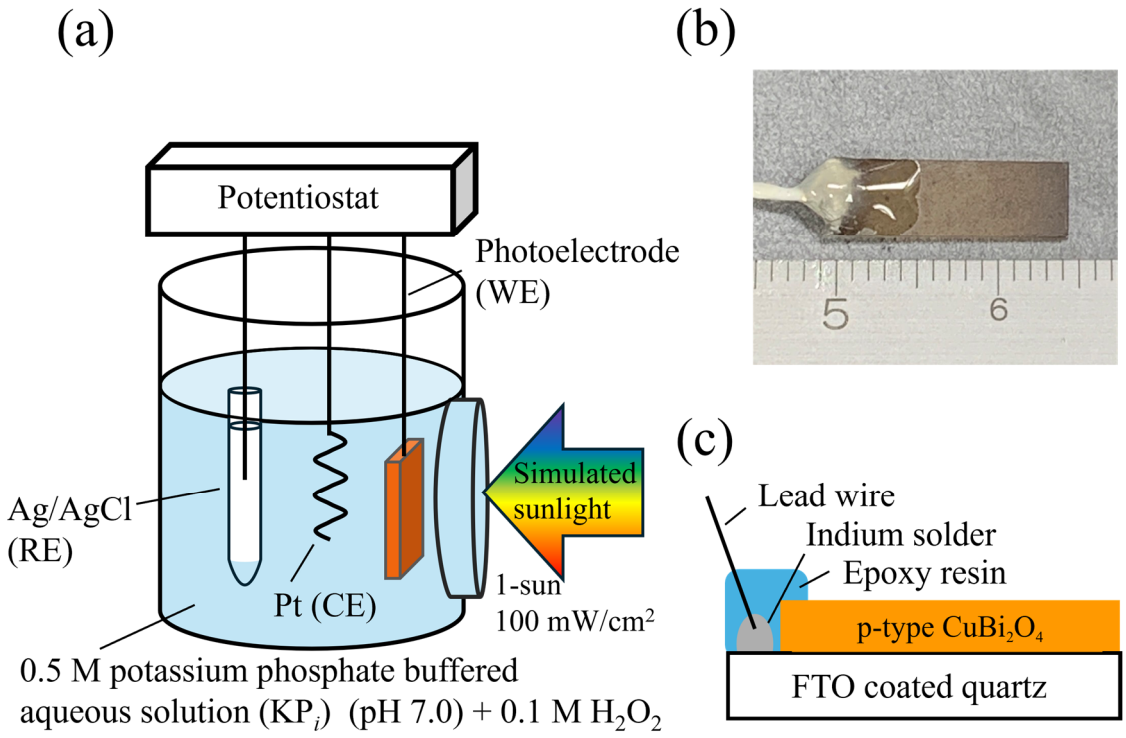

Figure S21. (a) Schematic illustration of photoelectrochemical (PEC) measurement with three-electrode configurations comprising of $CuBi_2O_4$/FTO/quartz photoelectrode (working electrode, WE), Ag/AgCl/sat'd KCl reference electrode (RE), and coiled Pt wire counter electrode (CE) under simulated AM 1.5G solar illumination (100 mW cm^{-2}). (b) Photograph of typical $CuBi_2O_4$/FTO/quartz photoelectrode. (c) cross-section structure of $CuBi_2O_4$/FTO/quartz photoelectrode. The lead wire was connected to the exposed FTO/quartz surface using indium solder, and then the unused region was covered with epoxy resin for insulation.

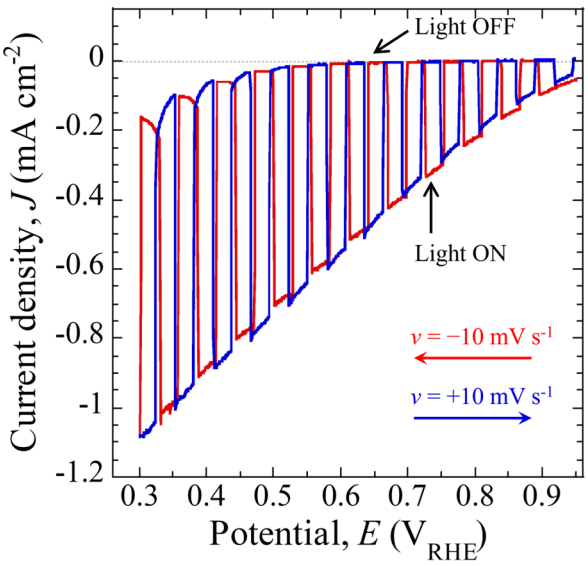

Figure S22. Photocurrent density-photoelectrode potential (*J*-*E*) curves of $CuBi_2O_4$/FTO photoelectrodes under chopped simulated AM 1.5G solar illumination (1 sun, 100 mW cm^{-2}). The potential sweep rate (v) and the electrolyte aqueous solution are 10 mV s^{-1} and 0.5 M KP_i + 0.1 M H_2O_2 (pH = 7.0), respectively. The *J*-*E* curves of the $CuBi_2O_4$ photoelectrodes showed the cathodic photocurrent in response to simulated sunlight irradiation, irrespective of the potential sweep directions: from positive to negative potentials (v = −10 mV s^{-1}, colored in red) and from negative to positive potentials (v = +10 mV s^{-1}, colored in blue).

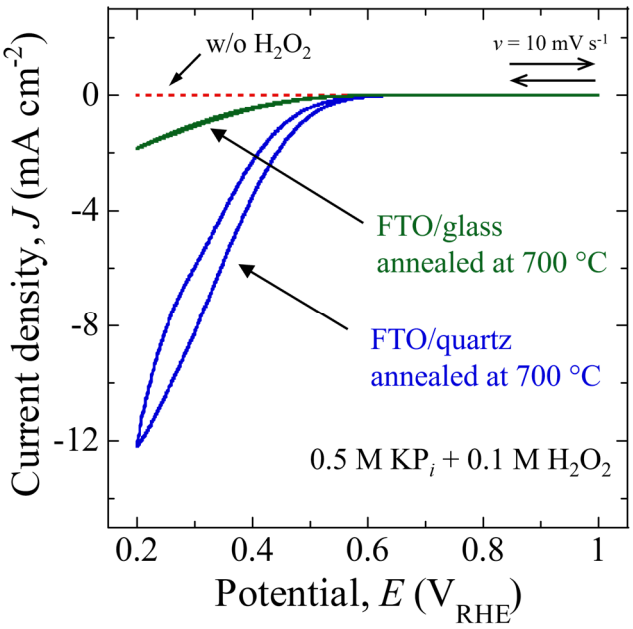

Figure S23. CV of bare-FTO/quartz (colored in blue) and bare-FTO/glass (colored in green) processed with post-annealing treatment at 700 °C for 1 h in air. The CV data was acquired in 0.5 M K-phosphate (KP_i) buffered aqueous solution (pH = 7.0, dotted line colored in red), and the addition of 0.1 M H_2O_2 sacrificial reagent (solid lines colored in blue and green). The CV data were obtained under an Ar gas atmosphere with a potential sweep rate (v) of 10 mV s^{-1} without stirring the electrolyte solution in the dark. The bare-FTO/quartz shows no cathodic current in the absence of an H_2O_2 sacrificial reagent in the measured electrode potential range. In the presence of an H_2O_2 sacrificial reagent, the bare-FTO/quartz generates the cathodic current attributable to the H_2O_2 reduction reaction. The onset potential on the H_2O_2 reduction reaction derived from the FTO/quartz is determined to be 0.55 V_{RHE}, which is more negative potential than that of the $CuBi_2O_4$/FTO/quartz photocathodes (onset potential of 1.05 V_{RHE}) under simulated AM 1.5G solar illumination, indicating that the p-type $CuBi_2O_4$ photocathode utilizes the photogenerated electron to H_2O_2 reduction reaction through the solar energy conversion process. The FTO/glass reference processed with a post-annealing treatment at 700 °C for 1 h shows the reduced cathodic current density derived from the H_2O_2 reduction reaction. The cathodic current density generated by FTO/quartz and FTO/glass at 0.2 V_{RHE} is found to be -12.2 mA cm^{-2} and -1.9 mA cm^{-2}, respectively.

References.

[1] M. Oshima and K. Yoshino, *Jpn. J. Appl. Phys.*, 2012, **51**, 125503.

[2] M. Oshima and K. Yoshino, *Jpn. J. Appl. Phys.*, 2011, **50**, 05FB15.